ADVANCED OPTICAL MATERIALS
www.advopticalmat.de

Noble Metal Free, Visible Light Driven Photocatalysis Using TiO_2 Nanotube Arrays Sensitized by P-Doped C_3N_4 Quantum Dots

Pawan Kumar, Piyush Kar, Ajay P. Manuel, Sheng Zeng, Ujwal K. Thakur, Kazi M. Alam, Yun Zhang, Ryan Kisslinger, Kai Cui, Guy M. Bernard, Vladimir K. Michaelis, and Karthik Shankar**

Bulk g-C_3N_4 is an earth-abundant, easily synthesizable, and exceptionally stable photocatalyst with an electronic bandgap of 2.7 eV. Herein, the concepts of P-doping and size quantization are combined to synthesize highly fluorescent P-doped carbon nitride quantum dots (CNPQDs) with a bandgap of 2.1 eV. CNPQDs are hosted on anatase-phase and rutile-phase TiO_2 nanotube array scaffolds, and examined as photoanodes for sunlight-driven water-splitting and as photocatalysts for surface catalytic reactions. Square-shaped rutile phase TiO_2 nanotube arrays (STNAs) decorated with CNPQDs (CNPQD-STNA) generate 2.54 mA cm^{-2} photocurrent under AM1.5 G simulated sunlight. A champion hydrogen evolution rate of 22 µmol h^{-1} corresponds to a Faradaic efficiency of 93.2%. In conjunction with Ag nanoparticles (NPs), the CNPQD-STNA hybrid is also found to be an excellent plexcitonic photocatalyst for the visible light-driven transformation of 4-nitrobenzenethiol (4-NBT) to dimercaptoazobenzene (DMAB), producing reaction completion at a laser power of 1 mW (532 nm) while Ag NP/TNA and Ag NP/STNA photocatalysts cannot complete this transformation even at 10 mW laser power. The results point the way forward for photochemically robust, noble metal free, visible light harvesting photoacatalysts based on nanostructured heterojunctions of graphenic frameworks with TiO_2.

1. Introduction

Sunlight assisted photoelectrochemical (PEC) water splitting is a powerful process for storing light energy in the chemical bonds of hydrogen, which is a portable fuel that can be ignited to release clean energy.[1] TiO_2 is an important semiconductor used as the photoanode for photoelectrochemical water splitting because of its chemical stability and the high oxidative power of its photogenerated holes. However, both the anatase and rutile forms of TiO_2 are wide bandgap (WBG) semiconductors, due to which TiO_2-based photocatalysts harvest <5% of the energy in the sun's spectrum, since the bulk of the solar energy reaching the earth's surface resides at visible and near-infrared wavelengths. The limited light harvesting abilities of stable, photocorrosion-resistant and earth-abundant metal oxide semiconductors (e.g., TiO_2, $SrTiO_3$, $NaNbO_3$, etc.) has prompted a major research effort into synthesizing new visible light-responsive semiconductors. One family of semiconductors that shows great promise for photocatalysis is that of graphenic semiconductors, which are conjugated polymers based on the substitution of one or more carbon atoms in the sp^2-hybridized graphene framework by nitrogen and other heteroatoms, which results in the opening of a bandgap.[2] Graphenic semiconductors are made of earth-abundant elements (C, N, O, etc.), have remarkable thermal and photochemical stability, adequate charge transport, and band edges and bandgaps that are tunable through molecular structure.[3] The most celebrated member of this family is bulk graphitic carbon nitride (g-C_3N_4; $E_g = 2.7$ eV), whose energy levels are well-matched with the requirements of water-splitting, CO_2 reduction and the degradation of numerous organic compounds.[4] In recent years carbon nitride quantum dots (CNQDs) are gaining popularity over conventional carbon/graphene quantum dots in various applications including sensing, bioimaging, chemical sensing, photocatalysis, etc. due to their excellent photochemical and thermal stability, nontoxic nature, and bright photoluminescence.[5]

Dr. P. Kumar, Dr. P. Kar, A. P. Manuel, S. Zeng, U. K. Thakur, Dr. K. M. Alam, Y. Zhang, R. Kisslinger, Prof. K. Shankar
Department of Electrical and Computer Engineering
University of Alberta
9211-116 St, Edmonton, Alberta T6G 1H9, Canada
E-mail: pawan@ualberta.ca; kshankar@ualberta.ca
Dr. K. Cui
Nanotechnology Research Centre
National Research Council of Canada
Edmonton, Alberta T6G 2M9, Canada
Dr. G. M. Bernard, Prof. V. K. Michaelis
Department of Chemistry
University of Alberta
Edmonton, Alberta T6G 2G2, Canada
The ORCID identification number(s) for the author(s) of this article can be found under https://doi.org/10.1002/adom.201901275.

DOI: 10.1002/adom.201901275

Two major problems with graphitic carbon nitride semiconductor electrodes whether constituted in the bulk or in the form of quantum dots or sheets, are limited light absorption and fast carrier recombination resulting in efficiency losses. A third problem is that some of the reactants in the aforementioned photocatalytic reactions adsorb poorly on the surfaces of graphenic semiconductors. The doping of carbon nitride materials with heteroatoms such as P, F, S, B, etc. has been reported to increase visible light absorption performance and photostability.[6] Phosphorus doping is particularly appealing where the P atoms substitute carbon in the tris-*s*-triazine (heptazine) ring system and participate in conjugation by donating an extra electron in the ring network leading to an electron rich, low bandgap carbon nitride framework.[7] Consequently, carbon nitride based semiconductors have been found to perform best as photocatalysts, when they are part of heterojunctions with other semiconductors such as TiO_2, ZnO, SnO_2, BiOBr, Fe_2O_3, $SrTiO_3$, etc.[8] In these heterojunctions, separation of photogenerated charge carriers is superior to stand-alone electrodes made of graphenic semiconductors, either due to facile photoinduced electron transfer or due to the formation of a Z-scheme. In addition, the strong adhesion of the graphenic semiconductor to a metal oxide semiconducting scaffold can also ameliorate the problem of leaching.

In this report, we present the synthesis of a graphenic semiconductor, namely phosphorus doped carbon nitride quantum dots (CNPQDs) via a facile thermal condensation polymerization reaction. We formed heterojunctions of CNPQDs with circular anatase and square-shaped rutile TiO_2 nanotube arrays (STNA) and investigated the resulting films as photoanodes for water splitting. Among the many different types of micro- and nanostructures of titanium dioxide used for photocatalytic applications, TiO_2 nanotube and nanowire arrays are uniquely suited as photoanodes for photoelectrochemical water-splitting due to their self-organized, highly ordered, vertically oriented geometry which enables orthogonalization of light harvesting and charge separation,[9] slow light and light trapping effects,[10] and directed pathways for the transport of electrons.[11] As mentioned in the previous paragraph, graphitic carbon nitride ($g\text{-}C_3N_4$) and related materials are a relatively new class of compounds, that have proven to be very effective in the photocatalytic field.[8d] From the photocatalytic standpoint, graphitic carbon nitride semiconductors are metal free and have interesting properties, including unique electrical and optical properties. Therefore, they can potentially eliminate the use of precious as well as toxic metals from photocatalytic devices.

2. Results and Discussion

2.1. Synthesis, Morphological, and Structural Characterization

The phosphorus doped CNPQDs were synthesized by solid state thermal condensation reaction of urea, citric acid, and 1-butyl-3-methylimidazolium hexafluorophosphate (BMIM-PF_6) at 200 °C in an autoclave by a slight modification of previously reported procedures (**Figure 1**a).[12] In this synthetic process, urea and citric acid react together via condensation polymerization to generate the basic carbon nitride framework while BMIM-PF_6 serves as the source of phosphorus doping.

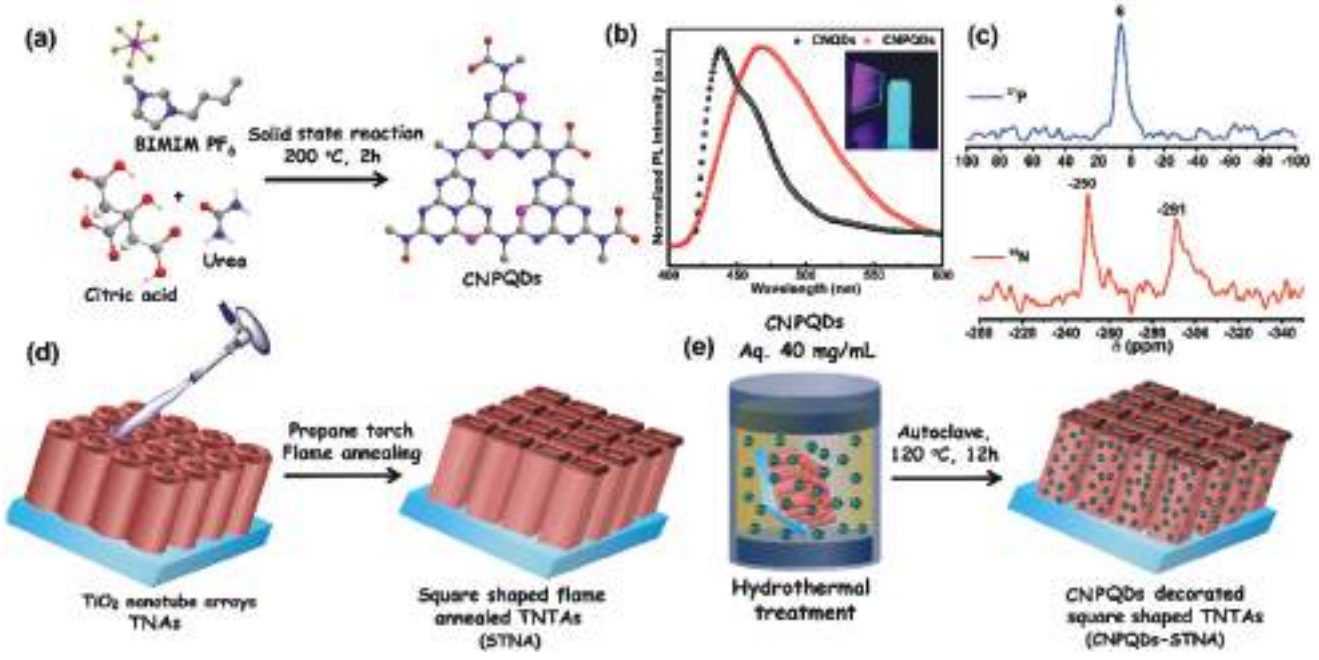

Figure 1. Schematic diagram illustrating the synthesis of a) phosphorus doped carbon nitride quantum dots (CNPQDs). b) Steady state photoluminescence (PL) spectrum of phosphorus doped carbon nitride quantum dots (CNPQDs) and carbon nitride quantum dots (CNQDs) in water (330 nm excitation wavelength). Inset showing fluorescence of CNPQDs sample under UV light irradiation. c) ^{15}N and ^{31}P CPMAS NMR spectra of CNPQDs. d) Flame annealed square shape TiO_2 nanotube arrays (STNAs) from aqueous TiO_2 nanotube arrays (TNAs). e) Hydrothermal treatment for decoration of CNPQDs on STNA (CNPQD-STNA) and TNA (CNPQD-TNA).

This protocol is different from conventional synthesis involving hydrothermal reaction of g-C_3N_4 QDs and phosphonitrilic chloride trimer.[13] The afforded CNPQDs show bright turquoise fluorescence under UV light irradiation. When excited by 330 nm photons, CNPQDs in water gave an intense broad photoluminescence (PL) peak centered at 462 nm as seen in Figure 1b, demonstrating emission at a longer wavelength than the previously reported PL for carbon nitride based quantum dots.[14] The observed redshifted PL suggests phosphorus doping increases the electronic charge density on the carbon nitride framework leading to a reduction in the bandgap due to the contribution of the extra electron from P to the heptazine ring system.[15] The UV–vis absorption spectrum of CNPQDs in water shows an intense peak at 300 nm corresponding to a $\pi \rightarrow \pi^*$ transition and another weak shoulder peak at 487 nm was assigned to $n \rightarrow \pi^*$ transition.[16] The presence of $n \rightarrow \pi^*$ transition at 487 nm demonstrates enhanced visible light absorption in comparison to previously reported carbon and carbon nitride quantum dots (Figure 4a).[12b,17] The synthesized CNPQDS were instantaneously dispersible in water which was attributed to their small size, electron rich surface (promoted by phosphorus doping), and the presence of ample amounts of amino and carboxylic moieties at the edge of the sheet-like quantum dots.[6a] To probe this assumption, the average particle size distribution and surface charge on CNPQDs were determined using dynamic light scattering (DLS) and zeta potential measurements, respectively. The average diameter of CNPQDs in water was found to be 28.12 nm (Figure S1, Supporting Information) while the surface potential was measured to be −20.1 mV (Figure S2, Supporting Information) which demonstrates extremely small size quantum dots and an electron rich surface decorated with −COOH/−NH_2 groups.[12c,18] The successful synthesis of carbon nitride quantum dots doped with phosphorous atoms was confirmed by solid-state nuclear magnetic resonance (NMR) spectroscopy acquired using the cross-polarization magic-angle spinning (CPMAS) technique (Figure 1c). The ^{15}N CPMAS NMR spectrum of CNPQDs reveals two NMR signals centered at −250 and −291 ppm. The ^{15}N NMR resonance centered between −240 and −270 ppm is attributed to secondary (NC_2) and tertiary (NC_3) nitrogen atoms of heptazine units constituting the carbon nitride skeleton while the peak located between −290 and −310 ppm is ascribed to primary nitrogens of terminal NH_2 groups.[19] These observed NMR resonances demonstrate the presence of a carbon nitride framework decorated with terminal NH_2 groups. A ^{31}P CPMAS NMR spectrum shows an intense peak at 6 ppm confirming the presence of doped phosphorous atoms in a carbon nitride scaffold as reported earlier.[7a,20] Additionally, a weak heptet signal was also observed at −145 ppm (not shown) attributed to a PF_6 phosphorous due to the presence of residual BMIM-PF_6.

Anatase phase TiO_2 nanotube arrays (TNAs) were prepared by electrochemical anodization of Ti foil in water-based electrolyte containing 4% v/v of hydrofluoric acid (HF) and 8% v/v of acetic acid followed by annealing at 450 °C for 3 h.[21] The obtained anatase phase TiO_2 nanotubes were subjected to high temperature annealing in a propane flame (≈750–900 °C) to afford rutile phase STNAs (Figure 1d).[21] The change in the cross-section of the nanotubes from circular to square, represents an interesting morphological change with important implications for the interaction of light with titania nanotubes.[22] Anatase phase TNA and flame annealed square-shaped TiO_2 nanotube array samples were decorated with CNPQDs via hydrothermal treatment at 120 °C for 12 h in an autoclave to obtain CNPQD-TNA and CNPQD-STNA nanostructures (Figure 1e).

Field emission scanning electron microscopy (FESEM) was used to determine the rough morphological attributes of TNAs and STNAs (Figure S3, Supporting Information). A typical FESEM image of TNA shows cylindrical nanotubes with an average diameter of 77 nm while cross-sectional view shows the nanotube to have an average length of 470 nm (Figure S3a,b, Supporting Information). The top-view of TiO_2 nanotubes after high temperature flame annealing (STNA) clearly shows the morphological transformation of cylindrical nanotubes into square-shaped nanotubes with 60–70 nm edge length (Figure S3c, Supporting Information) while cross-sectional view shows the average length of STNAs was ≈400 nm (Figure S3d, Supporting Information).

The ultrafine morphological attributes of phosphorus doped carbon nitride quantum dots decorated STNA samples (CNPQD-STNA) were investigated with high resolution transmission microscopy (HRTEM) (**Figure 2**). The HRTEM images of CNPQD-STNA at 10 nm scale bar show the presence of dark spots and amorphous region of CNPQDs on STNA (Figure 2a). The high magnification TEM images at 5 nm scale bar show lattice fringes with 0.33 and 0.27 nm interplanar d spacing corresponding to (110) and (101) planes of rutile phase TiO_2 (Figure 2b,c).[23] Another d spacing of 0.32 nm in HRTEM images was assigned to the (002) plane of carbonaceous materials demonstrating long range π–π stacking of CNPQDs on the surface of STNA (Figure 2c).[24] Further, HRTEM images show an unusually high d spacing of 0.63 nm, which were Moire fringes that originate in layered materials due to mismatched superimposition (dislocation or rotational) of two lattices with almost identical d spacing (Figure 2b).[25] The Moire fringe with almost double d spacing (0.63 nm) confirms presence of stacked CNPQDs on STNA.

Elemental mapping of CNPQD-STNA from top shows an even distribution of C, N, O, P, and Ti elements centered on the wall of nanotubes thus confirming the decoration of TiO_2 nanotubes with CNPQDs (Figure 2d). The presence of various peaks corresponding to C, N, O, P, Ti in the energy-dispersive X-ray (EDX) spectra of CNPQDs, further corroborate the decoration of STNA with CNPQDs (Figure 2e). To discern the presence of CNPQDs on STNA, electron energy loss (EEL) spectra of CNPQD-STNA samples were collected (Figure 2f). The EELS spectra display peaks corresponding to P *L*-edge, C *K*-edge, N *K*-edge, and Ti *L*-edge at 138.16, 287.14, 401.31, and 464.95 eV, respectively and reveal a chemically stable P-doped carbon nitride structure on the STNA.[26] The EELS mapping of sample shows well distributed concentration of C, N, and P over the nanostructures (Figure 2g). Further, EELS line scan mapping over nanotubes structures show intense signal of C, N, and P on the wall of TiO_2 nanotubes overlapped with Ti signals verifying the decoration of STNA with CNPQDs (Figure 2h).

The phase structure and crystalline nature of TNA and STNA samples with and without CNPQDs were investigated with X-ray diffraction (XRD) (Figure S6a, Supporting Information). The X-ray diffractogram of TNA sample was measured by

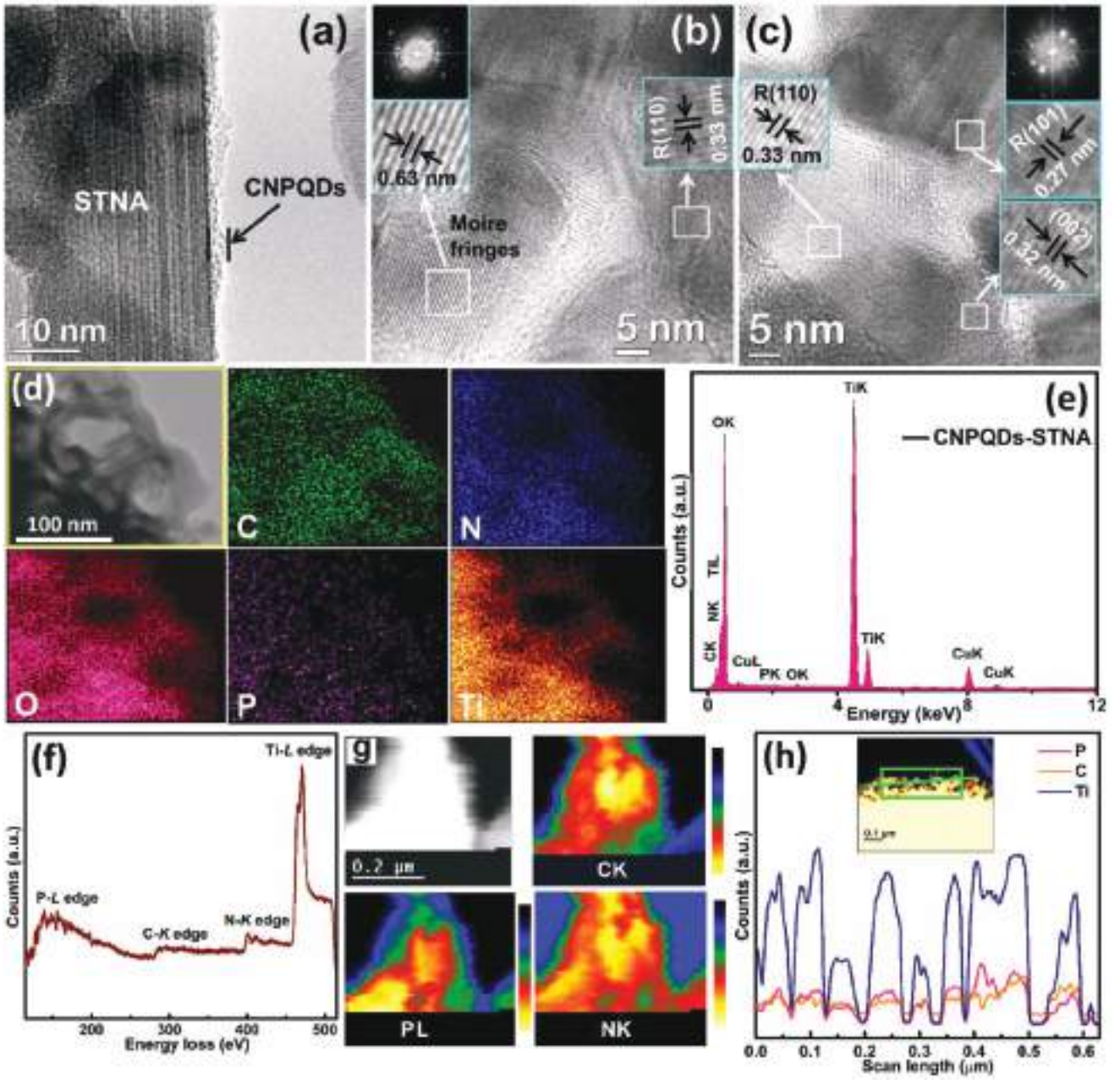

Figure 2. HRTEM images of CNPQD-STNA a) at 10 nm scale bar showing amorphous layers of CNPQDs deposited on STNA, b) at 5 nm scale bar showing lattice fringes and Moire fringes, insets shows rutile phase TiO_2 (110) plane d spacing and TEM FFT diffraction pattern, c) at 5 nm scale bar showing lattice fringes and insets shows rutile (110) and (101) planes d spacing and TEM FFT diffraction pattern. d) Bright field electron image, and STEM elemental maps for C, N, O, P and Ti. e) STEM-EDX spectra of CNPQD-STNA. f) Inner shell ionization edge (core loss) electron energy loss spectra (EELS) of CNPQD-STNA showing P-*L* edge, C-*K* edge, N-*K* edge, and Ti-*L* edge acquired on STEM. g) EELS elemental mapping of CNPQD-STNA showing map area, C-*K* edge, P-*L* edge and N-*K* edge. h) EELS line scan mapping of CNPQD-STNA for P (pink), C (orange) and Ti (navy blue) elements showing coinciding signal of P and N with Ti confirming decoration of STNA with CNPQDs.

maintaining a 2° angle between substrate and incident X-ray, and shows a diffraction peak at a 2θ value of 25.2°, which was assigned to the (101) plane of tetragonal anatase phase TiO_2 and matched well with JCPDS card #21-1272. Other peaks of TiO_2 were not distinguishable, likely due to the masking of signal from intense Ti substrate peaks. After decoration of CNPQDs on TNA, the peak intensity of (101) anatase peak decreased slightly suggesting coverage of TiO_2 surface with CNPQDs, which shields some signals. For STNA, the XRD peaks were observed at 27.3°, 36.0°, 41.2°, and 54.3° corresponding to (110) (101) and (111) and (211) planes of tetragonal rutile phase TiO_2 with a slightly orthorhombic distortion of the TiO_6 octahedron (JCPDS card #21-1276).[27] After hydrothermal treatment of STNA with CNPQDs under aqueous condition the peak intensities were

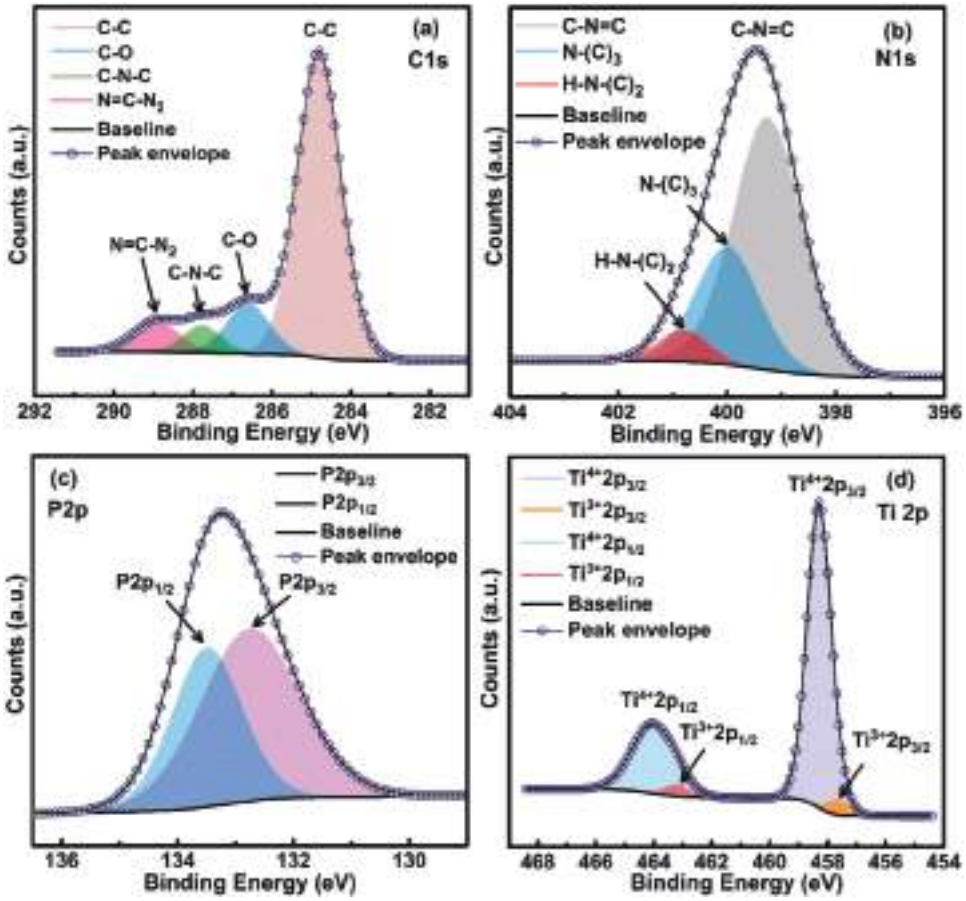

Figure 3. Core-level high resolution XPS spectra of CNPQD-STNA in a) C1s, b) N1s, c) P2p, and d) Ti2p regions.

decreased while a new peak was observed at ≈26° due to (002) reflection of stacked carbon nitride sheets which demonstrated the successful decoration of STNA with CNPQDs.[23]

To probe the presence of CNPQDs and measure the mode specific IR vibrational features, Raman spectra of the synthesized materials were collected (Figure S6b, Supporting Information). Raman spectra of TNA displayed the characteristic fingerprint bands of tetragonal anatase phase TiO_2 at 142.0, 396.1, 511.9, and 630.3 cm^{-1} indexed to E_g, B_{1g}, B_{1g}+A_{1g}, and E_g active modes.[28] After hydrothermal grafting of CNPQDs on the TNA in CNPQD-TNA, the intensity of these bands grew weaker and a few new bands at 450.1, 550.3, and 691.6 cm^{-1} appeared which were assigned to heptazine ring (tris-*s*-triazine, C_6N_7) breathing modes.[29] The presence of two signature peaks at 1358 and 1585 cm^{-1} attributed to the D and G bands of graphitic carbon based materials confirmed the presence of CNPQDs on the surface of TNA.[30] The D band signifying defects in the aromatic conjugated network originated due to out of plane vibration of sp^3 carbons while the G band peculiar to graphitic network originated due to in-plane vibrations of sp^2 carbons in the aromatic system.[31] The integral intensity ratio of D and G bands (I_D/I_G) was calculated to be 1.92 demonstrating plenty of defects present in the form of −COOH/C−NH_2 terminated functionalities on the heptazine nucleus.[32] Raman spectra of STNA exhibited IR active vibration bands at 138.2, 444.6, and 635 cm^{-1} assigned to B_{1g}, E_g, and A_{1g} modes of tetragonal rutile phase TiO_2 respectively while another less intense broad peak at 241.2 cm^{-1} was assigned to multiphonon processes.[33] The observation of weak anatase peaks in the Raman spectrum of STNA might be due to incomplete phase transformation during the flame annealing step. Analogous to CNPQD-TNA, the Raman spectra of CNPQD-STNA displayed a heptazine nucleus-specific peak at lower frequency and the characteristic D and G bands having an integral intensity ratio (I_D/I_G) of 1.84, which verified the presence of defect rich P-doped carbon nitride quantum dots over the surface of STNA.

The surface and sub-surface of chemical composition, and elemental oxidation states in CNPQD-TNA and CNPQD-STNA were probed using X-ray photoelectron spectroscopy (XPS) (**Figure 3**). The elemental survey scan of CNPQD-TNA and CNPQD-STNA exhibits C1s, N1s, O1s P2p, and Ti2p signal along with other inner-core excitation peaks confirms presence of all the constituting elements of CNPQDs and TiO_2 in material (Figure S8a, Supporting Information). Core-level high resolution XPS (HR-XPS) spectra of CNPQD-STNA in C1s region were deconvoluted into four peak components centered at 284.8, 286.6, 287.8, and 288.9 eV (Figure 3a). The peaks at 284.8 and 286.6 eV were assigned to sp^3 hybridized turbostratic carbons (C−C) and C−O carbons of carboxylic group, respectively.[34] Two other peak components located at BE ≈ 287.8 and 288.9 eV originated from sp^2 carbons in N=C−N_2 bonds and sp^3 carbon in C−N−C bonds which are basic constituents of the graphitic carbon nitride framework.

The HR-XPS of CNPQD-TNA displayed four peak components at 284.8, 286.5, 287.9, and 289.0 eV corroborated to C—C, C—O, N=C—N_2, and C—N—C type carbons, respectively (Figure S8b, Supporting Information). The HR-XPS of CNPQD-STNA and CNPQD-TNA in N1s region after deconvolution gave three peak components situated at BE ≈ 399.2, 400.0, and 400.8 eV which arose from secondary C—N=C, tertiary N—$(C)_3$ and primary H—N—$(C)_2$ type nitrogens, respectively (Figure 3b and Figure S8c, Supporting Information).[35] Further, deconvolution of P2p signals of CNPQD-STNA and CNPQD-TNA show two peak components at 132.4 and 133.4 eV due to $P2p_{3/2}$ and $P2p_{1/2}$ peak components of doped phosphorus. The presence of a single P2p peak with two orbital splitting components demonstrates that P atoms share an identical chemical environment in heptazine ring system and rules out the possibilities of P—O type phosphorous (Figure 3c and Figure S8d, Supporting Information).[36] The inner-core HR-XPS spectra of both CNPQD-STNA and CNPQD-TNA in Ti2p region consisted of two major peak components located at binding energies of 458.6 and 464.4 eV, which were assigned to $Ti2p_{3/2}$ and $Ti2p_{1/2}$ peak components of Ti^{4+} state in TiO_2 nanocrystals (Figure 3d and Figure S8e, Supporting Information).[37] The 5.8 eV peak splitting between $Ti2p_{3/2}$ and $Ti2p_{1/2}$ peaks and their respective positions was in well agreement with Ti^{4+} coordinated to O^{2-} (Ti^{4+}-O^{2-}) in the TiO_6 octahedron of tetragonal TiO_2 crystals.[38] Additionally, Ti2p XPS spectra of CNPQD-STNA and CNPQD-TNA displayed two weak shoulder peaks at relatively lower BE ≈ 457.7 and 463.2 eV originated from $Ti2p_{3/2}$ and $Ti2p_{1/2}$ peak components of Ti^{3+} present in the form of lattice defects.[39] The flame annealing of TiO_2 samples tends to create Ti^{3+} defects and oxygen vacancies due to abstraction of lattice oxygens at high temperature which generates sub gap energy levels just below the conduction band (shallow traps) resulting in a slight narrowing of the bandgap.[40] In our previous reports we have demonstrated that STNA possesses a higher density of defects in comparison to TNA which promotes a better visible light response and enhanced photocatalytic performance in the photoreduction to CO_2 to methane.[41] The O1s peak of CNPQD-STNA and CNPQD-TNA split into two peak components positioned at 529.5 and 531.6 eV (Figures S7 and S8f, Supporting Information). The peak at 529.5 eV was attributed to oxygen atoms in the crystal lattice of TiO_2 (Ti–O–Ti) while the peak at 531.6 eV originated from the contribution of surface adsorbed non-lattice —OH in TiO_2 and C=O and —OH of carboxylic groups on the surface of CNPQDs (Figures S7 and S8f, Supporting Information). XPS results clearly demonstrate the presence of intact phosphorus doped carbon nitride quantum dots on the surface of tetragonal TiO_2.

2.2. Optical Properties and Electronic Band Structure

The optical absorption performance of materials was determined using UV–vis absorption spectra collected in diffuse reflectance mode (**Figure 4**). The CNPQDs show $\pi \rightarrow \pi^*$ and $n \rightarrow \pi^*$ transition peaks centered at 300 and 487 nm, respectively revealing visible light absorbance (Figure 4a).[16a] It is noteworthy that the optical absorption of CNPQDs reported in this work with a band edge at ≈600 nm (Figure 4a) is significantly different from the absorption behavior of N, P-codoped carbon dots which exhibited a band edge at ≈450 nm.[42] The emission peak of CNPQDs occurs at 462 nm (λ_{exc} = 330 nm) as shown in Figure 1b while N, P-codoped carbon dots exhibit excitation-dependent emission behavior with a PL emission maximum at 410 for 330 nm excitation.[42] The DR UV–vis spectrum of TNA displayed the semiconductor band edge of anatase at ≈385 nm (Figure 4b). The weak yet broad absorption feature centered at ≈450 nm arose due to the presence of mid-gap states due to oxygen vacancies creating deep level traps facilitating longer wavelength absorption.[43] The flame annealing of TNA at elevated temperature transformed anatase phase TiO_2 into rutile phase TiO_2 in STNA and UV–vis absorption edge was red-shifted by ≈25 to 410 nm corresponding to the 3.0 eV bandgap of rutile. After decoration of CNPQDs on TNA and STNA, the visible light absorption performances of CNPQD-TNA and CNPQD-STNA were enhanced with each type of sample showing maximum absorption in between 460 to 550 nm.

The electronic structure and band edge energies of materials with respect to vacuum level were calculated from ultraviolet photoelectron spectroscopy (UPS) work function (WF) spectra and valence band spectra acquired using UPS (Figure 4). The value of work function was calculated by subtracting the energy of emitted secondary electrons ($E_{cut\text{-}off}$) from the incident energy of UV light source (He laser: 21.21 eV) using the following expression WF (ϕ) = 21.21−$E_{cut\text{-}off}$. The cut-off energy was determined from the point of intersection of the extrapolated linear region of work function on *X* and *Y* scale. From the WF spectra, the $E_{cut\text{-}off}$ energies of TNA, STNA, CNPQD-TNA, and CNPQD-STNA were estimated to be 16.91, 16.71, 16.89, and 16.63 eV, respectively which correspond to WF values of 4.30, 4.50, 4.32, and 4.58 eV, respectively (Figure 4c). From the work function value, it was obvious that Fermi level of STNA was 0.20 eV below the Fermi level of TNA which demonstrate transformation of anatase phase TiO_2 in TNA to rutile phase TiO_2 in STNA during high temperature annealing. The obtained Fermi level values and 0.20 eV energy difference was in close agreement with literature values.[44] After decoration of CNPQDs on TNA and STNA, the position of Fermi level was not changed significantly which suggests that the formation of an electronic heterojunction between TiO_2 and CNPQDs did not result in band bending. Further, linear extrapolation of the leading edges in UPS valence band spectra gave the position of valance band maxima (VBM) (Figure 4d). The VBM positions for TNA and STNA were calculated to be 3.21 and 3.11 eV, respectively. The CNPQD-TNA, CNPQD-STNA displayed two valence band edges corresponding to CNPQDs and TiO_2 suggesting that in the CNPQD-TiO_2 nanocomposite, each material retains its individual electronic identity. The VBM edge values for CNFQDs-TNA were found to be 2.70 and 1.32 eV while CNPQD-STNA displayed VB position at 2.97 and 2.42 eV assigned to TiO_2 and CNPQDs respectively.

2.3. Performance of CNPQD Decorated Titania Nanotubes in Photoelectrochemical Water Splitting

Photoelectrochemical water splitting experiments were performed in a three-electrode configuration wherein the bare/heterojunction TiO_2 nanotube array scaffold on Ti foil was assigned

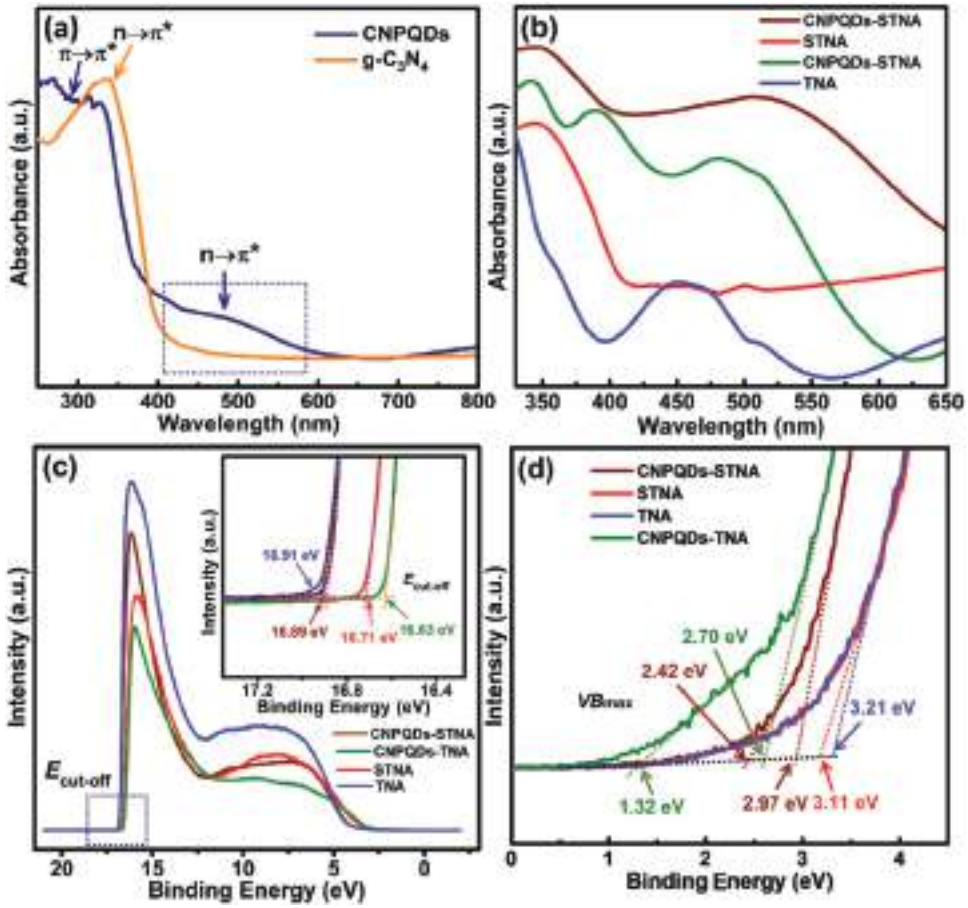

Figure 4. a) UV–vis spectra of CNPQDs in water showing $\pi \rightarrow \pi^*$ and $n \rightarrow \pi^*$ transition and UV–vis spectra of bulk g-C_3N_4. b) Diffuse reflectance UV–vis spectra of TNA, CNPQD-TNA, STNA, and CNPQD-STNA. c) UPS work function spectra of TNA, CNPQD-TNA, STNA, CNPQD-STNA and inset shows cut-off energy ($E_{cut\text{-}off}$) of secondary electrons. The work function (WF) was determined from the UPS work function spectra using the equation WF (ϕ) = 21.21 − $E_{cut\text{-}off}$, where 21.21 eV is energy of the incident, He discharge lamp used for UPS. d) UPS valence band spectra of TNA, CNPQD-TNA, STNA, CNPQD-STNA showing the estimated values of the respective valence band maxima below the Fermi level. Color: TNA (blue), CNPQD-TNA (green), STNA (red) and CNPQD-STNA (wine red).

as the photoanode (working electrode) while Pt was used as photocathode (counter electrode) and the voltage bias was applied with respect to an Ag/AgCl reference electrode. All three electrodes were immersed in 1 M KOH electrolyte and the photoanode was irradiated with AM1.5 G one sun simulated sunlight. The photocurrent response, expressed in the terms of the photocurrent density, was measured in linear sweep voltammetric (LSV) mode by sweeping the applied bias from −0.8 to +1.0 V versus Ag/AgCl. In the dark, almost zero photocurrent density was observed for each of the tested samples (**Figure 5**a–e). Under one sun illumination, all samples showed appreciable photocurrents at an applied bias of +0.6 V versus Ag/AgCl (1.23 V vs RHE equivalent to water oxidation potential). Pristine TNA and STNA samples achieved current densities of 0.04 and 0.30 mA cm^{-2}, respectively under simulated sunlight passed through a 420 nm UV cut-off filter while the current densities without the UV cut-off filter were found to be 0.17 and 0.75 mA cm^{-2}, respectively, at +0.6 V versus Ag/AgCl. The photocurrent response of STNA was 7.5 and 4.4 times higher than TNA under one sun irradiation with UV filter (>420 nm) and without UV filter respectively. These results clearly demonstrate the superior photoelectrochemical performance of STNA due to the presence of the lower bandgap (3.0 eV) rutile phase in comparison to anatase phase TiO_2 (3.2 eV) in TNA. Further, Ti^{3+} defects and oxygen vacancies were responsible for the visible light response of materials. The enhancement of water splitting performance was also due to shortened carrier collection pathways, because of the short (in length) and thin walled STNA formed in aqueous electrolyte. In order to make the most of the finite carrier mobility and charge carrier lifetime, short aqueous nanotubes with thin walls are well suited. Recombination is minimized before charge carriers reach the interface with the electrolyte, and before the electrons reach the Ti foil on their way to the external circuit. As we shall show in the next section (finite-difference time-domain (FDTD) simulations), the square-shaped pore morphology also results in more effective absorption of photons in both bare and CNPQD-decorated TiO_2 nanotubes.[45]

The photocurrents generated by TNA and STNA samples were tremendously increased after decoration of CNPQDs (Figure 5a,b). The measured photocurrent densities for CNPQD-TNA and CNPQD-STNA under solar simulated light with UV filter (>420 nm) were calculated to be 0.24 and 0.45 mA cm^{-2}

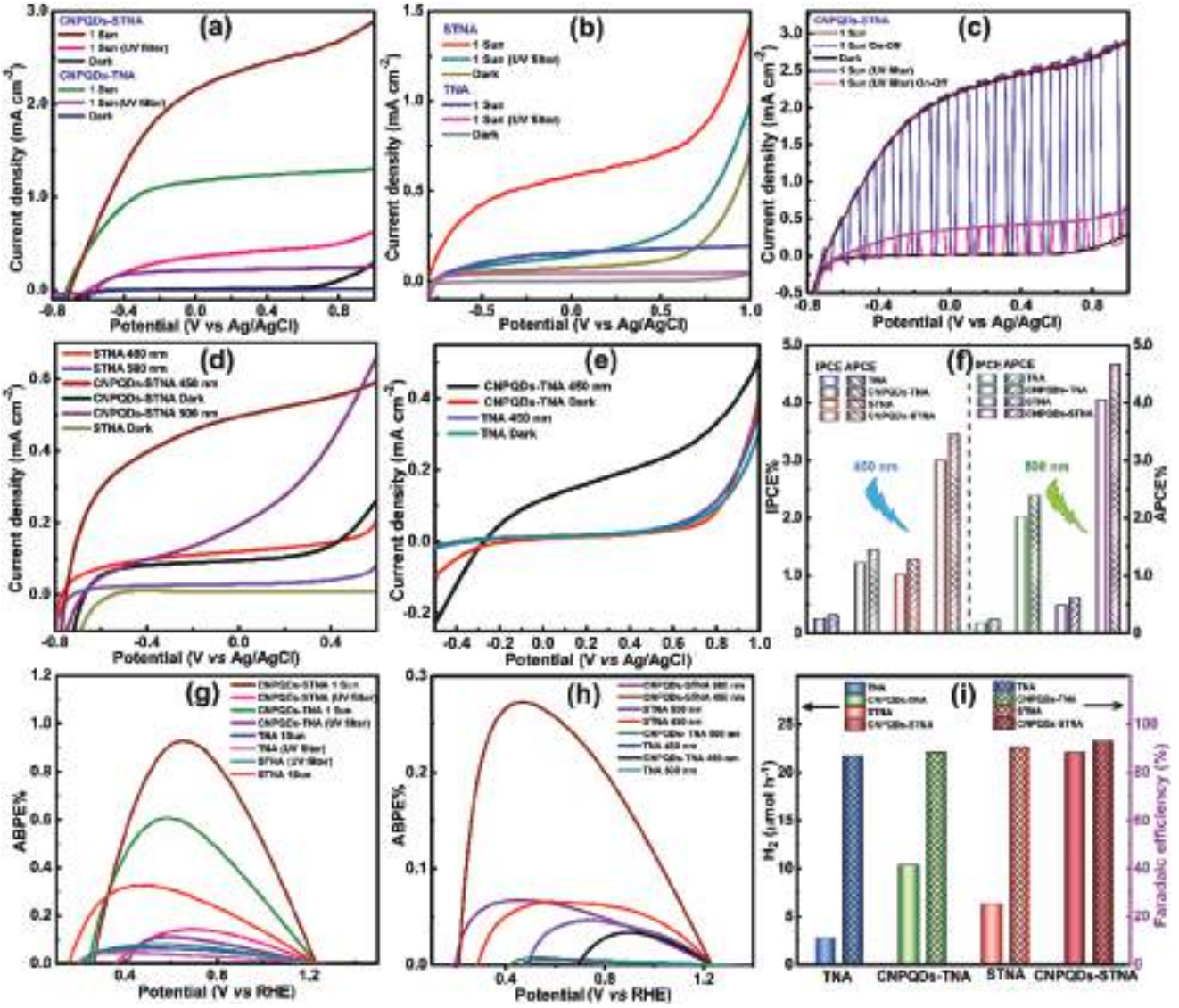

Figure 5. Photocurrent density versus applied potential plot for a) CNPQD-STNA and CNPQD-TNA. b) STNA and TNA. c) Photocurrent density change during light on-off cycle for CNPQD-STNA under dark conditions, under solar simulated AM1.5 G irradiation with 420 nm cut-off filter, under AM1.5 G irradiation without UV cut-off filter. d) Photocurrent density versus applied potential plot for STNA and CNPQD-STNA under dark conditions, under 450 nm LEDs irradiation (power density 54.15 mW cm^{-2}) and 500 nm LEDs irradiation (power density 40.58 mW cm^{-2}). e) TNA, CNPQD-TNA under dark conditions, under 450 nm LEDs irradiation (power density 54.15 mW cm^{-2}). f) IPCE and APCE% of TNA, CNPQD-TNA, STNA, CNPQD-STNA samples in 450 and 500 nm wavelength LED. Plot between ABPE% versus potential showing maximum ABPE% of TNA, STNA, CNPQD-TNA, CNPQD-STNA g) under solar simulated AM1.5 G irradiation (>420 nm), under AM1.5 G irradiation without UV cut-off filter h) under 450 nm wavelength LEDs irradiation, under 500 nm wavelength LEDs irradiation. All the measurements were carried out in 1.0 M KOH solution at a scan rate of 0.1 mV s^{-1}. i) Bar diagram showing experimentally observed H_2 evolution rate and corresponding Faradaic efficiencies using TNA, CNPQD-TNA, STNA CNPQD-STNA samples under AM1.5 G irradiation.

while without UV filter, the photocurrent densities were found to be 1.26 and 2.54 mA cm^{-2}, respectively. CNPQD-STNA show the highest photocurrent density which was 1.9 times higher than CNPQD-TNA under AM1.5 G irradiation (>420 nm) and 2.0 times without UV filter. The photocurrent response of materials during light On–Off cycles exhibited evident peaks and troughs and confirms the photoresponse of the materials to be real and not an artifact of the scan rate (Figure 5c) The photoelectrochemical performance of the samples under near-monochromatic illumination at discrete longer wavelengths was tested using 450 and 500 nm light emitting diodes (LEDs) with power densities of 54.15 and 40.58 mW cm^{-2} at the surface of the samples (Figure 5d). The relative photocurrent density of STNA based samples was highest among all samples. The photocurrent densities of STNA and CNPQD-STNA samples under 450 nm irradiation were found to be 0.20 and 0.59 mA cm^{-2} while under 500 nm irradiation the value of photocurrent densities were measured to be 0.08 and 0.65 mA cm^{-2}, respectively (Figure 5d). Under identical conditions TNA and CNPQD-TNA samples displayed 0.04 and 0.24 mA cm^{-2} current density at 450 nm

(Figure 5e). Under 500 nm wavelength illumination, the current densities of TNA and CNPQD-TNA were measured to be 0.05 and 0.32 mA cm^{-2}. The calculated current density of CNPQD-STNA was 8.1 and 13.0 times higher than bare STNA and TNA respectively at 500 nm wavelength. Diagnostic efficiencies of materials were estimated to investigate materials system/interface performance (Section S2, Supporting Information).[1a,46] This is a proof of concept study intended to showcase the potential of CNPQDs decorated on nanostructured n-type semiconducting scaffolds as visible light harvesting photonodes for sunlight-driven water splitting. Therefore, neither the nanotube length nor the total loading of CNPQDs was optimized for maximum performance. The applied bias photoconversion efficiency (ABPE) measures the overall conversion of light into electricity, and ABPE values approaching 1% were obtained for the unoptimized systems presented in this study under AM1.5 G one sun illumination (Figure 5g). A particularly relevant metric consists of the absorbed photon-to-electron conversion efficiency (APCE) at visible wavelengths which measures the internal quantum yield of conversion of incident photons into electrons that generate current in the external circuit. APCEs as high as 3.5% for 450 nm photons and 4.7% for 500 nm photons, were achieved using CNPQD-STNA samples (Figure 5f). The results of hydrogen evolution experiments using H-cells (Figure S14, Supporting Information) indicated a champion H_2 production rate of 22 µmol h^{-1} corresponding to a Faradaic efficiency of 93.2% (Figure 5h and Section S2, Supporting Information).

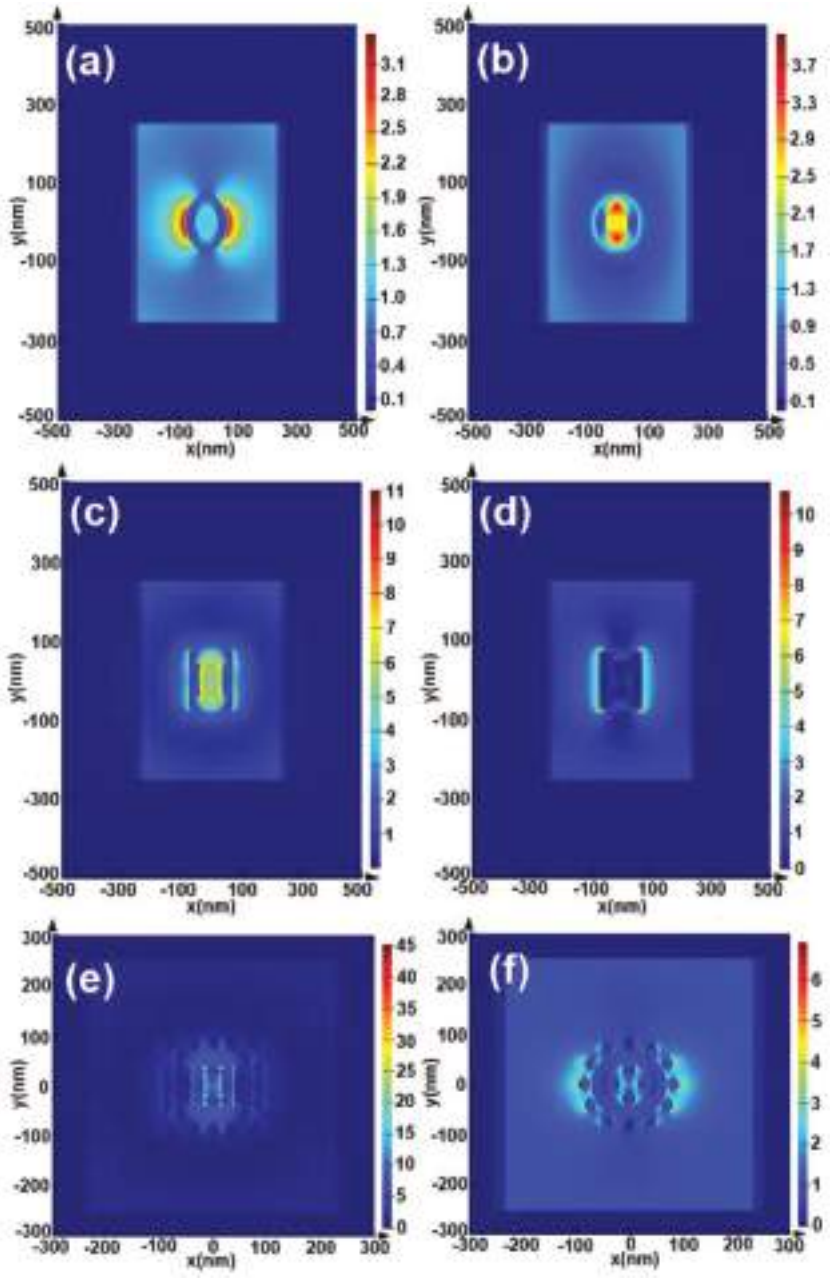

Figure 6. Results of FDTD simulations of discrete titania nanotubes showing electric field intensities for a) TNAs at 500 nm. b) TNAs at 350 nm. c) STNAs at 500 nm. d) STNAs at 350 nm. e) CNPQD-STNA at 500 nm. f) CNPQD-TNA at 500 nm.

2.4. FDTD Simulations of TNAs, STNAs, CNPQD-TNAs, and CNPQD-STNAs

Both cylindrical and square cross-sectioned titania nanotubes can behave as symmetric hollow core waveguides for incident photons in sunlight due to the large refractive index contrast between the high index TiO_2 annulus and the surrounding air medium.[47] In **Figure 6**a, we see that for bare cylindrical anatase-phase TNAs, the electric field intensity at 500 nm does not decrease exponentially in the air cladding. The fundamental mode is almost cut-off as the electric field spreads into the air medium surrounding the nanotubes. For 350 nm photons, the waveguiding effect of the cylindrical nanotubes is strong in spite of the bandgap absorption of TiO_2 as evidenced by a strong electric field that is fully confined within the hollow core of the nanotube (Figure 6b). On the other hand, 350 nm photons are almost fully attenuated due to absorption by TiO_2 in bare rutile-phase square nanotubes (STNAs) with a small evanescent field at the outer wall of the nanotubes (Figure 6d). STNAs also exhibit a strong confinement of the electric field for 500 nm photons within the hollow core with an exponential decrease in the field intensity outside the nanotubes (Figure 6c). Following decoration of the STNAs with CNPQDs, the electric field intensity at the top of the square nanotubes is dramatically weaker and the optical energy is confined to a much smaller volume within the nanotubes due to the rapid attenuation of light because of absorption by the CNPQDs. In contrast, the circular TNAs when decorated with CNPQDs still show an appreciable electric field intensity

at the outer edge of the concentric nanotube-CNPQD hybrid. These results indicate the CNPQD-STNAs to be significantly more efficient absorbers of visible light (particularly photons with wavelengths of 350–500 nm) than CNPQD-TNAs and demonstrate the importance of nanotube shape in determining the interactions with light.

It is well-known that the optical spectra of sub-micrometer long titania nanotubes exhibit pronounced optical interference fringes due to reflections from the air-TNA and substrate-TNA interfaces.[48] Indeed, the simulated cross-sectional electric field profiles of both CNPQD-TNA and CNPQD-STNA show undulating intensities due to constructive and destructive interference (Figure S10a,b,d,e, Supporting Information). However, the CNPQD-STNA samples (Figures S10d and S13e, Supporting Information) are indicated to attenuate the electric field intensity much more strongly in comparison to CNPQD-TNA samples (Figure S10a,b, Supporting Information), thus demonstrating the enhanced light harvesting ability of square-shaped mixed phase titania nanotube samples decorated with P-doped g-C_3N_4 quantum dots. The simulated optical spectra indicate absorption [1–(*R*+*T*)] peaks at 395 and 530 nm for CNPQD-TNA and corresponding absorption troughs at 365 and 440 nm (Figure S10c, Supporting Information). In the experimentally measured UV–vis spectrum of CNPQD-TNA (green curve in Figure 4b), we see an absorption peak at 390 nm and a broad absorption feature centered at ≈500 nm along with absorption troughs at 365 and 440 nm. Thus, the FDTD simulations capture an impressive number of features seen in the measured UV–vis spectrum of CNPQD-TNA while also confirming that the overall absorptance of the CNPQD-STNA samples is significantly higher than that of CNPQD-TNA samples in the 350–550 nm spectral range.

2.5. Plausible Mechanism of Enhanced Photoelectrochemical Water Splitting Performance

To obtain greater insight into the superior photoelectrochemical performance of CNPQD-STNA, we have proposed a plausible mechanism (**Figure 7**) based on experimental findings on electronic band structure and existing literature. The minimum requirement for efficient water splitting without any sacrificial donor on a semiconductor surface is a more negative CB position than the proton reduction potential (0.00 eV vs NHE at pH-0; H^+/H_2) and a more positive valence band position than the water oxidation potential (+1.23 eV vs NHE at pH-0; H_2O/O_2).[49] This implies that the bandgap value of the semiconductor should be more than 1.23 eV with appropriate values of the electronic band edges. Regular furnace annealed TNA is composed of anatase TiO_2 (E_g = 3.2 eV) which absorbs only UV light (λ < 386 nm) and cannot drive water splitting reaction in the visible regime. However, the presence of defects and mid-gap states that originated in the anodization process and were not completely healed during annealing, enables longer wavelength absorption which is evident from the absorption band at 450 nm in the UV–vis spectrum of TNA.[43a,50] However, these traps are detrimental to the water splitting process due to the annihilation of photogenerated charge carriers via trap assisted recombination.[51] This explained the low observed photocurrent density and low ABPE for TNA samples under

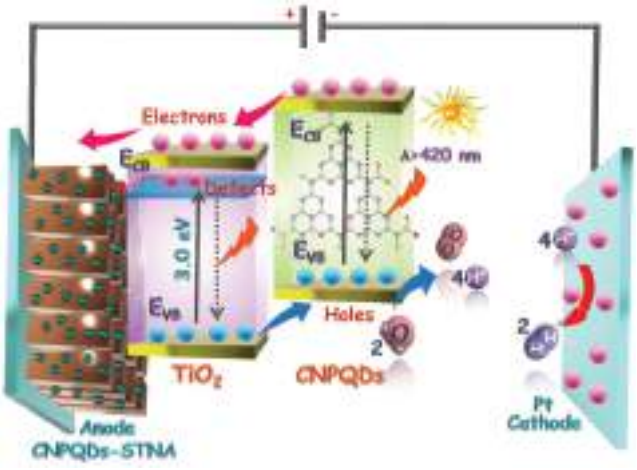

Figure 7. Mechanistic scheme of photoelectrochemical water splitting on CNPQD-STNA nanohybrid.

irradiation from the 450 nm LED (blue curve in Figure 5b,e). The flame annealing of TNA samples at elevated temperature results in the transformation of anatase TiO_2 into rutile phase TiO_2 in STNA with a band-edge at 410 nm. The ≈25 nm redshift in the band-edge enables STNAs to harvest a significant fraction of violet and blue photons, and results in the generation of photocurrent densities of ≈0.75 mA cm^{-2} at +0.6 V versus Ag/AgCl by bare, undecorated STNA samples (cyan curve in Figure 5b). Work function spectra indicate that the Fermi level of rutile phase TiO_2 in STNA lies 0.2 eV lower than anatase phase TiO_2 in good agreement with literature values.[44] After decoration by phosphorus doped CNPQDs, the photoelectrochemical performance was dramatically increased to 2.54 mA cm^{-2} (red color in Figure 5a–e) which was due to enhanced harvesting of visible light by CNPQDs coupled with efficient injection of photogenerated electrons from the CB of CNPQDs to the CB of TiO_2.[8a] Therefore photosensitization was indicated to be the leading mechanism in photocatalysis. The resulting electrons in the conduction band of TiO_2 moved to the Pt cathode through the external circuit to reduce water while the holes at photoanode facilitated water oxidation. Despite the similar geometric dimensions of TNA and STNA, the CNPQD-STNA samples exhibited photocurrents that were 100% larger than those obtained using CNPQD-TNA samples. This large difference in performance was primarily attributable to two reasons. The 0.2 eV lower CB position in rutile phase STNA compared to anatase phase facilitated electron injection from the CNPQDs into STNA and enabled higher internal quantum yields. Secondly, the square-shaped morphology of the STNAs played a role in enhancing light-matter interactions (Figure 6 and Figure S10, Supporting Information). The overall water splitting reaction can be expressed as follow

$$4OH^- + 4h^+ \rightarrow O_2 + 2H_2O \text{ at anode} \quad (1)$$

$$4H_2O + 4e^- \rightarrow 2H_2 + 4OH^- \text{ at counter electrode} \quad (2)$$

High photoelectrochemical performance by a semiconductor photoanode such as shown in Figure 5a,c is only possible

when the photogenerated holes are efficiently transferred to the hydroxyl ions in the aqueous electrolyte per Equation (1). In carbon nitride quantum dots, secondary and tertiary N atoms bonded to C constitute the highest occupied molecular orbital (HOMO) (equivalent to valence band) while the π-conjugated system behaves like the conduction band lowest unoccupied molecular orbital (LUMO).[4d,52] Phosphorus doping takes place by replacement of ring carbons with phosphorus which contributes loosely held extra electron to the conjugated network resulting in the uplifting of the VB and reduction of bandgap.[7a,37] It is clear from this work that P-doped C_3N_4 quantum dots are able to efficiently transfer holes to electrolyte species.

2.6. Photoreduction of 4-Nitrobenzenethiol (4-NBT) to Dimercaptoazobenzene (DMAB)

Harvesting solar energy to drive surface catalytic reactions is an enticing protocol due to their benign environment-friendly nature and use of unexhaustive energy resource. Recently plasmonic materials coupled with semiconductor or graphenic materials has shown wide potential in plasmon-exciton (collectively called "plexciton") co-driven surface catalytic reaction due to a synergistic improvement in plasmon-to-electron conversion efficiency.[53] In this venture, plasmonic nanoparticles (NPs) integrated with semiconductor photocatalysts such as Cu_2O,[54] MoS_2,[55] TiO_2,[50b,51] graphitic carbon nitride (g-C_3N_4),[56] doped and undoped graphene,[53d,57] etc. have been explored for the surface photocatalytic conversion of aromatic thiols into azo compounds.[58] To probe the feasibility of CNPQDs decorated TiO_2 nanotubes to drive surface catalytic reactions, the photocatalytic reduction of 4-NBT into *p,p′*-dimercaptoazobenzene was chosen as a model reaction and the progress of the reaction was monitored by surface-enhanced Raman spectroscopy (SERS) using a 532 nm laser. Prior to measurement, 10 nm Ag was sputtered on to the samples followed by deposition of 4-NBT and laser power was varied from 0.1 to 10.0 mW to obtain the laser power dependent degradation of 4-NBT to DMAB. **Figure 8**a shows the normal Raman spectra of pristine 4-NBT and DMAB along with comparative SERS spectra of 4-NBT adsorbed Ag sputtered glass, TNA, STNA, CNPQD-TNA, and CNPQD-STNA samples at 1.0 mW incident laser power. The Raman spectrum of 4-NBT contains three signature peaks at 1101, 1332, and 1576 cm^{-1} corroborated to S−C stretch, NO_2 vibration and C=C stretch respectively while the Raman spectrum of DMAB has peaks at 1142 (C=N stretch), 1389 and 1438 cm^{-1} (N=N stretch).[53d,59] After irradiation with 532 nm laser at a laser power 1.0 mW, bare Ag nanoparticles on glass substrate show negligible change in Raman signal demonstrating plasmonic silver alone was incapable to reduce 4-NBT (Figure 8b). Likewise, 4-NBT adsorbed Ag coupled bare TNA samples showed a small decrease in peak intensity of N−O vibration at 1576 cm^{-1} and appearance of new peaks corresponding to DMAB A_{1g} mode at 1142 (C−N stretch), 1389 and 1438 (N=N stretch) cm^{-1}, respectively, revealing that a very small fraction of 4-NBT was reduced to DMAB at 1 mW laser power (Figure 8c). However, for Ag NP coupled STNA samples a significant drop in N−O peak intensity at 1576 cm^{-1} was observed along with a rise in the amplitude of the DMAB peaks which confirmed the better photocatalytic performance of STNA (Figure 8d). After decoration by CNPQDs, poorly performing TNA exhibited excellent conversion of 4-NBT to DMAB (Figure 8e). Using CNPQD-TNA and CNPQD-STNA, almost complete conversion of 4-NBT to DMAB was attained at a low laser power of 1 mW while bare Ag NPs, Ag NP/TNA, and Ag NP/STNA were unable to complete the transformation from 4-NBT to DMAB even at 10 mW laser power (Figure 8e). From these observations it can be concluded that CNPQDs decoration of TNA and STNA dramatically amplifies photocatalytic performance. Prior reports show that graphene and graphenic frameworks are highly effective at extracting hot electrons from the plasmon decay in silver nanostructures.[3d,60] Therefore, a higher plasmon-to-electron conversion efficiency on CNPQDs leads to increased hot electron-density to facilitate high catalytic conversion. In addition, the long interaction times of harvested hot electrons with phonons in graphenic frameworks[61] improves the rate of phonon-driven catalysis.

3. Conclusion

Phosphorus doping of bulk graphitic carbon nitride (g-C_3N_4) has been previously demonstrated to narrow the bandgap of g-C_3N_4 from 2.7 to 1.7 eV. We synthesized P-doped g-C_3N_4 quantum dots (CNPQDs) with an average size of 28 nm using a facile and scalable solid-state thermal condensation polymerization reaction method. The CNPQDs were found to have a negatively charged surface with a zeta potential of −20 mV and were easily dispersed in water. CNPQDs had an enlarged bandgap of 2.1 eV and exhibited a more red-shifted photoluminescence (λ_{max} = 478 nm) in comparison to other reported carbon nitride/carbon quantum dots. The CNPQDs were hosted on anodically formed titania nanotube array scaffolds to create heterojunction photocatalysts. The titania nanotubes had an average diameter of 70 nm and a tube-length of ≈0.5 µm. Two distinct types of titania nanotube supports were used for decoration with CNPQDs— anatase phase cylindrical TNA and rutile phase STNA. The TNA and STNA samples significantly differed in their interactions with light both prior to, and following decoration with CNPQDs. Optical FDTD simulations indicated the STNAs to exhibit a lesser waveguiding effect for UV photons than TNAs and provide a stronger confinement of 500 nm photons than TNAs while displaying a higher density of hot spots. These differences enabled CNPQD-STNAs to perform enhanced light harvesting in comparison to CNPQD-TNAs, as confirmed by experimentally measured optical absorption spectra. When used as photoanodes for sunlight-driven water splitting, CNPQD-STNAs generated a photocurrent density as high as 2.54 mA cm^{-2} at +0.6 V versus Ag/AgCl while achieving significant quantum yields for wavelengths as long as 500 nm. The resulting hydrogen generation rate was measured to be 22 µmol h^{-1}, which corresponded to a Faradaic efficiency as high as 93.2%. When loaded with sputtered Ag NPs, the CNPQD-STNAs were transformed into plexcitonic photocatalysts due to the interaction of the plasmonic and excitonic resonances in the weak coupling regime. Ag NP/CNPQD-STNAs were demonstrated to be excellent visible light-driven photocatalysts by completing

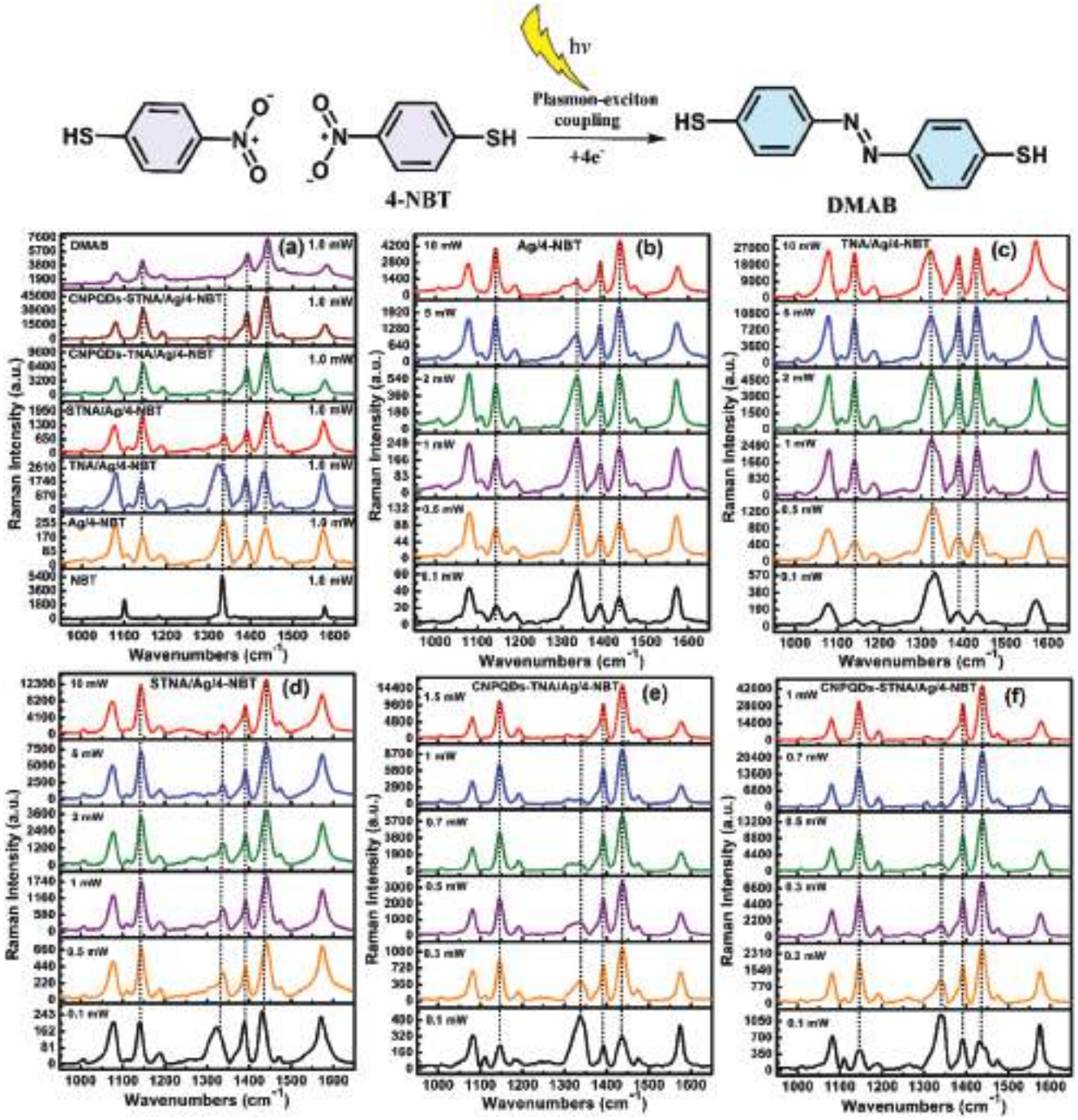

Figure 8. Schematic showing plexcitonic surface catalytic reduction of 4-nitrobenzenethiol (4-NBT) to DMAB (*p,p′*-dimercaptoazobenzene) and a) Raman spectra of pristine 4-NBT (black), DMAB (purple) and comparison of SERS spectra of plexcitonic surface catalytic transformation of 4-NBT to DMAB on bare Ag (orange),10 nm Ag sputtered TNA (blue), STNA (red), CNPQD-TNA (green), CNPQD-STNA (wine red) under 532 nm laser illumination at 1 mW power, and SERS spectra of plasmon-exciton co-induced surface catalytic degradation of 4-NBT to DMAB as function of laser power on a) 10 nm Ag sputtered on glass, c) 10 nm Ag sputtered TNA, d) 10 nm Ag sputtered STNA, e) 10 nm Ag sputtered CNPQD-TNA, f) 10 nm Ag sputtered CNPQD-STNA.

the photoreduction of 4-NBT to *p,p′*-dimercaptoazobenzene at a laser power of 1 mW at 532 nm whilst Ag NP/STNAs could not complete the photoreduction even at a laser power of 10 mW at 532 nm, thus confirming the importance of the coupling between the Ag NPs and CNPQDs in generating high photocatalytic performance.

4. Experimental Section

Synthesis of Phosphorus Doped CNPQDs: The phosphorus doped CNPQDs were synthesized by solid-phase thermal condensation of urea, citric acid, and BMIM-PF_6 by slight modification of previously reported procedures.[12] In this synthesis procedure, citric acid and urea work as the source of carbon and nitrogen respectively to form the carbon nitride

framework while BMIM-PF_6 furnishes phosphorus for intentional doping. Briefly, 1.94 g citric acid (10 mmol) and 3.60 g urea (60 mmol) were mixed together in an agate mortar followed by addition of 1.0 g BMIM-PF_6 (7.0 mmol). The afforded mixture was transferred into a 50 mL Teflon lined stainless steel autoclave and heated at 200 °C for 2 h to achieve condensation polymerization and phosphorus doping. After cooling to room temperature, the obtained solid was washed with dichloromethane to remove unreacted organics, followed by extraction in water. The obtained solution was centrifuged at 12 000 rpm to sediment large particles.

Synthesis of TNA and STNAs: TNA samples were prepared by electrochemical anodization of Ti foil using an aqueous electrolyte recipe. The water-based electrolyte was composed of 4% v/v of HF and 8% v/v of acetic acid. The anodization was carried out at room temperature using a two-electrode system containing a graphite cathode and Ti anode with an applied voltage of 15 V between the Ti anode and graphite cathode. The obtained TiO_2 nanotube samples were annealed at 450 °C under air for three hours. The samples were denoted as TNA. The TNA samples were subjected to flame annealing at an elevated temperature (≈750–900 °C) using a propane torch for 2 min. The obtained flame annealed samples due to their specific square shape was denoted as flame annealed square-shaped TiO_2 nanotubes array.

Synthesis of CNPQD-TNA and CNPQD-STNAs: For the synthesis of CNPQD decorated TNA photocatalyst, 15 mL of CNPQDs (20 mg mL^{-1}) was added to a 50 mL Teflon lined autoclave. To this solution Ti foil having TiO_2 nanotube arrays (TNA and STNA) were immersed and keep standing vertically. Autoclave was put in an oven at 120 °C for 12 h for hydrothermal treatment. After cooling to room temperature, the CNPQDs decorated TiO_2 samples were withdrawn and washed with deionized water and methanol. The obtained samples were dried at 60 °C and used for photoelectrochemical measurements.

Measurement of Photoelectrochemical Water Splitting Performance: To perform photoelectrochemical water splitting experiment three electrode system composed of bare and CNPQDs decorated TiO_2 samples as photoanode (working electrode), Pt cathode (counter electrode) and Ag/AgCl reference electrode system, respectively, was immersed in 0.1 M KOH electrolyte. To stimulate a photoresponse, AM1.5 G simulated sunlight from a Newport Oriel solar simulator (model 67 005) equipped with a Class A filter was used and the power density on the surface of samples was maintained at 100 mW m^{-2}. To probe the visible light response of materials, the photocurrent was measured in response to AM1.5 G simulated sunlight passed through a 420 nm cut-off filter. Further, to determine the photoresponse behavior of samples at discrete visible wavelengths and calculate quantum efficiencies, experiments were carried out using 450 and 500 nm wavelength LEDs, having 54.15 and 40.48 mW cm^{-2} power densities at the surface of the sample, respectively. The photocurrent was measured by linear sweep voltammetry by sweeping applied voltage from −0.8 to +1.0 V versus Ag/AgCl. The intensities of illumination from the LEDs on the sample surface were calibrated with a photodiode. Additionally, dark current was also measured for comparing the photoresponse of samples. The gaseous sample from the Pt electrode containing arm was withdrawn after 30 min interval using a gas tight syringe and analyzed using a gas chromatographs (GC)–pulse discharge detector (PDD) system. The gaseous products of photoelectrochemical water splitting were identified and quantified using gas chromatography on a custom-made Shimadzu GC equipped with Porapak Q column and Mol Sieve column, and a PDD. Conditions: He carrier flow rate: 0.5 mL min^{-1}, detector temperature: 160 °C, oven temp: started from 60 °C and raised up to 160 °C. For the quantification of gaseous hydrogen, a standard gas mixture (Praxair gas, Canada) was used as a calibration standard.

Measurement of the Activity for Surface Catalytic Reactions: Prior to measurement, 10 nm Ag was sputtered on the samples. For comparison 10 nm Ag was also sputtered on glass. A methanolic solution of 4-NBT (5×10^{-5} M) was drop-casted on the Ag sputtered samples followed by drying in a vacuum oven at room temperature. The photocatalytic performance of samples in plasmon-exciton co-promoted surface photocatalytic reduction of 4-NBT to DMAB was determined using surface-enhanced Raman scattering (SERS) spectroscopy on a Thermo Scientific DXR2 Raman Microscope with a 532 nm laser by varying laser power from 0.1 to 10 mW. The SERS spectra were acquired using a 50 µm pinhole aperture size, 2 µm spot size and 2 cm^{-1} per CCD pixel element 900 lines mm^{-1} spectral dispersion grating. The spectra were accumulated for 3×25 s.

Optical Simulations: Optical properties of the cylindrical and square nanotube structures were investigated using Lumerical FDTD simulation software. The nanotubes were simulated with circular and square cross-sections with inner and outer radii of 40 and 70 nm, respectively, and a height of 300 nm. The simulations were performed for both combinations of individual nanotubes in a vacuum environment, as well as nanotubes decorated by nitrogen-doped C_3N_4 quantum dots with radii of 12 nm. Scattering and absorption cross-sections, electric field intensity profiles, Poynting vector distributions, as well as reflection and transmission spectra were captured using near and far-field profile and frequency monitors.

Material compositions of rutile (square) and anatase (cylindrical) TiO_2 nantoubes were simulated using appropriate refractive index data as obtained via ellipsometry. An additional set of refractive index data corresponding to anatase TiO_2 was also obtained from Siefke et al.[62] Refractive index data corresponding to N@C quantum dots was obtained from Kumar et al.[63] with the resulting stand-alone simulations of N@C quantum dot nanoparticles displaying absorption spectrum profiles identical to the UV–vis absorption spectra of the N@C quantum dots utilized in experiments. Lumerical's refractive index monitor confirmed the structures were appropriately configured and identified by the software throughout the course of the simulation. The structures were illuminated by a light source incident at a normal angle from above with a bandwidth of 350–800 nm. Snapshots of the electric field intensity profiles, and Poynting vector distributions were taken at selective wavelengths between 300–600 nm, and as observed along different planes including the *xy*-, *xz*-, and *yz*-planes. Appropriate symmetric and antisymmetric boundaries were considered given the symmetry of the nanotube structures, and allowed for shorter simulation times, and accurate data aggregation.

Supporting Information

Supporting Information is available from the Wiley Online Library or from the author.

Acknowledgements

All authors thank the Natural Sciences and Engineering Research Council (NSERC), the National Research Council (NRC), Future Energy Systems, and CMC Microsystems for direct and indirect (equipment use) financial support. Scholarship supports from Alberta Innovates to U.K.T., and from NSERC to R.K. and A.P.M. are acknowledged. Some device fabrication and testing used research infrastructure made possible by a Leaders Opportunity Fund grant to K.S. from the Canada Foundation for Innovation and matched by the Alberta Small Equipment Grants Program. The authors acknowledge use of the following user-fee based characterization facilities: The Cell Imaging Facility, the Oil Sands and Coal Interfacial Engineering Facility, and the University of Alberta nanoFab.

Conflict of Interest

The authors declare no conflict of interest.

Author Contributions

P.K. and P.K. contributed equally to this work. P.K. and P.K. synthesized and characterized the materials and performed photoelectrochemical water splitting experiments. A.P.M. performed FDTD simulation studies.

U.K.T. conducted the electrochemical characterization of materials. K.M.A. helped in collection of characterization data and also performed the 4-NBT photoreduction experiments. Y.Z. helped in the synthesis of nanotubes for the studies. R.K. helped in imaging and EDX analysis of samples. K.C. performed HRTEM, elemental mapping and EELS on samples. S.Z. assisted in calibration of LEDs and calculation of efficiencies. K.S. supervised the research and edited the manuscript. G.M.B. and V.K.M. performed the solid-state NMR experiments.

Keywords

carbon nitride quantum dots, hydrogen generation, metal-free catalysts, nanotubes, semiconductor photoelectrocatalysis

Received: July 28, 2019
Revised: October 15, 2019
Published online:

[1] a) Z. Chen, H. N. Dinh, E. Miller, *Photoelectrochemical Water Splitting*, Springer, New York **2013**; b) J. Stringer, L. Horton, Basic Research Needs to Assure a Secure Energy Future, *Oak Ridge, TN, Oak Ridge National Laboratory*, US Department of Energy **2003**, pp. A-97–A-101.

[2] a) H. Wang, T. Maiyalagan, X. Wang, *ACS Catal.* **2012**, *2*, 781; b) A. Lherbier, X. Blase, Y.-M. Niquet, F. Triozon, S. Roche, *Phys. Rev. Lett.* **2008**, *101*, 036808.

[3] a) J. Liu, Y. Liu, N. Liu, Y. Han, X. Zhang, H. Huang, Y. Lifshitz, S.-T. Lee, J. Zhong, Z. Kang, *Science* **2015**, *347*, 970; b) X. Wang, K. Maeda, A. Thomas, K. Takanabe, G. Xin, J. M. Carlsson, K. Domen, M. Antonietti, *Nat. Mater.* **2009**, *8*, 76; c) D. Masih, Y. Ma, S. Rohani, *Appl. Catal., B* **2017**, *206*, 556; d) P. Kumar, E. Vahidzadeh, U. K. Thakur, P. Kar, K. M. Alam, A. Goswami, N. Mahdi, K. Cui, G. M. Bernard, V. K. Michaelis, K. Shankar, *J. Am. Chem. Soc.* **2019**, *141*, 5415.

[4] a) F. K. Kessler, Y. Zheng, D. Schwarz, C. Merschjann, W. Schnick, X. Wang, M. J. Bojdys, *Nat. Rev. Mater.* **2017**, *2*, 17030; b) P. Kumar, R. Boukherroub, K. Shankar, *J. Mater. Chem. A* **2018**, *6*, 12876; c) M. Volokh, G. Peng, J. Barrio, M. Shalom, *Angew. Chem., Int. Ed.* **2019**, *58*, 6138; d) W.-J. Ong, L.-L. Tan, Y. H. Ng, S.-T. Yong, S.-P. Chai, *Chem. Rev.* **2016**, *116*, 7159.

[5] a) Y. Tang, Y. Su, N. Yang, L. Zhang, Y. Lv, *Anal. Chem.* **2014**, *86*, 4528; b) H. Li, F.-Q. Shao, H. Huang, J.-J. Feng, A.-J. Wang, *Sens. Actuators, B* **2016**, *226*, 506; c) Q. Cui, J. Xu, X. Wang, L. Li, M. Antonietti, M. Shalom, *Angew. Chem., Int. Ed.* **2016**, *55*, 3672.

[6] a) L. Jiang, X. Yuan, Y. Pan, J. Liang, G. Zeng, Z. Wu, H. Wang, *Appl. Catal., B* **2017**, *217*, 388; b) Y. Wang, Y. Di, M. Antonietti, H. Li, X. Chen, X. Wang, *Chem. Mater.* **2010**, *22*, 5119; c) J. P. Paraknowitsch, A. Thomas, *Energy Environ. Sci.* **2013**, *6*, 2839; d) K. M. Alam, P. Kumar, P. Kar, U. K. Thakur, S. Zeng, K. Cui, K. Shankar, *Nanoscale Adv.* **2019**, *1*, 1460.

[7] a) Y. Zhang, T. Mori, J. Ye, M. Antonietti, *J. Am. Chem. Soc.* **2010**, *132*, 6294; b) Y.-P. Zhu, T.-Z. Ren, Z.-Y. Yuan, *ACS Appl. Mater. Interfaces* **2015**, *7*, 16850.

[8] a) J. Su, L. Zhu, G. Chen, *Appl. Catal., B* **2016**, *186*, 127; b) Z. Zhao, Y. Sun, F. Dong, *Nanoscale* **2015**, *7*, 15; c) C. Chang, L. Zhu, S. Wang, X. Chu, L. Yue, *ACS Appl. Mater. Interfaces* **2014**, *6*, 5083; d) J. Wen, J. Xie, X. Chen, X. Li, *Appl. Surf. Sci.* **2017**, *391*, 72; e) G. Mamba, A. Mishra, *Appl. Catal., B* **2016**, *198*, 347; f) C. Ott, F. Reiter, M. Baumgartner, M. Pielmeier, A. Vogel, P. Walke, S. Burger, M. Ehrenreich, G. Kieslich, D. Daisenberger, *Adv. Funct. Mater.* **2019**, *29*, 1900233; g) J. Xu, I. Herraiz-Cardona, X. Yang, S. Gimenez, M. Antonietti, M. Shalom, *Adv. Opt. Mater.* **2015**, *3*, 1052; h) B. Chai, T. Peng, J. Mao, K. Li, L. Zan, *Phys. Chem. Chem. Phys.* **2012**, *14*, 16745; i) L. Zhang, D. Jing, X. She, H. Liu, D. Yang, Y. Lu, J. Li, Z. Zheng, L. Guo, *J. Mater. Chem. A* **2014**, *2*, 2071.

[9] a) K. Shankar, J. I. Basham, N. K. Allam, O. K. Varghese, G. K. Mor, X. Feng, M. Paulose, J. A. Seabold, K.-S. Choi, C. A. Grimes, *J. Phys. Chem. C* **2009**, *113*, 6327; b) K. R. Reyes-Gil, D. B. Robinson, *ACS Appl. Mater. Interfaces* **2013**, *5*, 12400.

[10] a) X. Zhang, F. Han, B. Shi, S. Farsinezhad, G. P. Dechaine, K. Shankar, *Angew. Chem., Int. Ed.* **2012**, *51*, 12732; b) G. L. Chiarello, A. Zuliani, D. Ceresoli, R. Martinazzo, E. Selli, *ACS Catal.* **2016**, *6*, 1345.

[11] A. Mohammadpour, P. Kar, B. D. Wiltshire, A. M. Askar, K. Shankar, *Curr. Nanosci.* **2015**, *11*, 593.

[12] a) P. Kumar, U. K. Thakur, K. Alam, P. Kar, R. Kisslinger, S. Zeng, S. Patel, K. Shankar, *Carbon* **2018**, *137*, 174; b) J. Zhou, Y. Yang, C.-y. Zhang, *Chem. Commun.* **2013**, *49*, 8605; c) Y.-C. Lu, J. Chen, A.-J. Wang, N. Bao, J.-J. Feng, W. Wang, L. Shao, *J. Mater. Chem. C* **2015**, *3*, 73.

[13] J. Wu, S. Yang, J. Li, Y. Yang, G. Wang, X. Bu, P. He, J. Sun, J. Yang, Y. Deng, G. Ding, X. Xie, *Adv. Opt. Mater.* **2016**, *4*, 2095.

[14] a) N. Wang, H. Fan, J. Sun, Z. Han, J. Dong, S. Ai, *Carbon* **2016**, *109*, 141; b) W. Wang, C. Y. Jimmy, Z. Shen, D. K. Chan, T. Gu, *Chem. Commun.* **2014**, *50*, 10148; c) Q. Liang, W. Ma, Y. Shi, Z. Li, X. Yang, *Carbon* **2013**, *60*, 421.

[15] B. Chai, J. Yan, C. Wang, Z. Ren, Y. Zhu, *Appl. Surf. Sci.* **2017**, *391*, 376.

[16] a) J. Zhang, X. Chen, K. Takanabe, K. Maeda, K. Domen, J. D. Epping, X. Fu, M. Antonietti, X. Wang, *Angew. Chem., Int. Ed.* **2010**, *49*, 441; b) A. Kumar, P. Kumar, C. Joshi, S. Ponnada, A. K. Pathak, A. Ali, B. Sreedhar, S. L. Jain, *Green Chem.* **2016**, *18*, 2514.

[17] a) S. Barman, M. Sadhukhan, *J. Mater. Chem.* **2012**, *22*, 21832; b) Y. Dong, H. Pang, H. B. Yang, C. Guo, J. Shao, Y. Chi, C. M. Li, T. Yu, *Angew. Chem.* **2013**, *125*, 7954.

[18] T. T. Meiling, P. J. Cywiński, I. Bald, *Sci. Rep.* **2016**, *6*, 28557.

[19] a) B. V. Lotsch, M. Döblinger, J. Sehnert, L. Seyfarth, J. Senker, O. Oeckler, W. Schnick, *Chem. - Eur. J.* **2007**, *13*, 4969; b) B. Jürgens, E. Irran, J. Senker, P. Kroll, H. Müller, W. Schnick, *J. Am. Chem. Soc.* **2003**, *125*, 10288; c) A. Schwarzer, U. Böhme, E. Kroke, *Chem. - Eur. J.* **2012**, *18*, 12052; d) X. Li, I. V. Sergeyev, F. Aussenac, A. F. Masters, T. Maschmeyer, J. M. Hook, *Angew. Chem.* **2018**, *130*, 6964; e) Y. Hu, Y. Shim, J. Oh, S. Park, S. Park, Y. Ishii, *Chem. Mater.* **2017**, *29*, 5080; f) Y. Wang, Y. Li, W. Ju, J. Wang, H. Yao, L. Zhang, J. Wang, Z. Li, *Carbon* **2016**, *102*, 477.

[20] a) X.-X. Fang, L.-B. Ma, K. Liang, S.-J. Zhao, Y.-F. Jiang, C. Ling, T. Zhao, T.-Y. Cheang, A.-W. Xu, *J. Mater. Chem. A* **2019**, *7*, 11506; b) S. Guo, Z. Deng, M. Li, B. Jiang, C. Tian, Q. Pan, H. Fu, *Angew. Chem., Int. Ed.* **2016**, *55*, 1830.

[21] a) P. Kar, Y. Zhang, S. Farsinezhad, A. Mohammadpour, B. D. Wiltshire, H. Sharma, K. Shankar, *Chem. Commun.* **2015**, *51*, 7816; b) P. Kar, Y. Zhang, N. Mahdi, U. K. Thakur, B. D. Wiltshire, R. Kisslinger, K. Shankar, *Nanotechnology* **2017**, *29*, 014002.

[22] P. Kar, S. Zeng, Y. Zhang, E. Vahidzadeh, A. Manuel, R. Kisslinger, K. M. Alam, U. K. Thakur, N. Mahdi, P. Kumar, K. Shankar, *Appl. Catal., B* **2019**, *243*, 522.

[23] S. Yang, Y. Gong, J. Zhang, L. Zhan, L. Ma, Z. Fang, R. Vajtai, X. Wang, P. M. Ajayan, *Adv. Mater.* **2013**, *25*, 2452.

[24] Y. Zheng, Z. Zhang, C. Li, *J. Photochem. Photobiol., A* **2017**, *332*, 32.

[25] Y. Liao, W. Cao, J. W. Connell, Z. Chen, Y. Lin, *Sci. Rep.* **2016**, *6*, 26084.

[26] a) D. H. Park, K. S. Lakhi, K. Ramadass, M. K. Kim, S. N. Talapaneni, S. Joseph, U. Ravon, K. Al-Bahily, A. Vinu, *Chem. - Eur. J.* **2017**, *23*, 10753; b) L. F. Chen, Z. H. Huang, H. W. Liang, H. L. Gao, S. H. Yu, *Adv. Funct. Mater.* **2014**, *24*, 5104.

[27] a) H.-S. Kim, J.-W. Lee, N. Yantara, P. P. Boix, S. A. Kulkarni, S. Mhaisalkar, M. Grätzel, N.-G. Park, *Nano Lett.* **2013**, *13*, 2412;

b) E. Hosono, S. Fujihara, K. Kakiuchi, H. Imai, *J. Am. Chem. Soc.* **2004**, *126*, 7790.
[28] a) C. Ratanatawanate, C. Xiong, K. J. Balkus Jr., *ACS Nano* **2008**, *2*, 1682; b) T. Ohsaka, F. Izumi, Y. Fujiki, *J. Raman Spectrosc.* **1978**, *7*, 321.
[29] Y. Kang, Y. Yang, L. C. Yin, X. Kang, G. Liu, H. M. Cheng, *Adv. Mater.* **2015**, *27*, 4572.
[30] M. Y. Chen, D. Li, X. Lin, V. Dravid, Y. W. Chung, M. S. Wong, W. D. Sproul, *J. Vac. Sci. Technol., A* **1993**, *11*, 521.
[31] P. Cheng, Z. Yang, H. Wang, W. Cheng, M. Chen, W. Shangguan, G. Ding, *Int. J. Hydrogen Energy* **2012**, *37*, 2224.
[32] S. Kumar, P. Kumar, S. L. Jain, *J. Mater. Chem. A* **2014**, *2*, 18861.
[33] D. Eder, A. H. Windle, *Adv. Mater.* **2008**, *20*, 1787.
[34] a) Q. Liang, Z. Li, X. Yu, Z. H. Huang, F. Kang, Q. H. Yang, *Adv. Mater.* **2015**, *27*, 4634; b) Z. Song, T. Lin, L. Lin, S. Lin, F. Fu, X. Wang, L. Guo, *Angew. Chem., Int. Ed.* **2016**, *55*, 2773.
[35] a) A. Kumar, P. Kumar, R. Borkar, A. Bansiwal, N. Labhsetwar, S. L. Jain, *Carbon* **2017**, *123*, 371; b) N. Hellgren, R. T. Haasch, S. Schmidt, L. Hultman, I. Petrov, *Carbon* **2016**, *108*, 242.
[36] J. Ran, T. Y. Ma, G. Gao, X.-W. Du, S. Z. Qiao, *Energy Environ. Sci.* **2015**, *8*, 3708.
[37] X. Chen, Q. Liu, Q. Wu, P. Du, J. Zhu, S. Dai, S. Yang, *Adv. Funct. Mater.* **2016**, *26*, 1719.
[38] J. Park, T. Back, W. C. Mitchel, S. S. Kim, S. Elhamri, J. Boeckl, S. B. Fairchild, R. Naik, A. A. Voevodin, *Sci. Rep.* **2015**, *5*, 14374.
[39] J. Chen, W. Song, H. Hou, Y. Zhang, M. Jing, X. Jia, X. Ji, *Adv. Funct. Mater.* **2015**, *25*, 6793.
[40] a) M. S. Hamdy, R. Amrollahi, G. Mul, *ACS Catal.* **2012**, *2*, 2641; b) S. G. Ullattil, P. Periyat, *J. Mater. Chem. A* **2016**, *4*, 5854.
[41] P. Kar, S. Zheng, Y. Zhang, E. Vahidzadeh, A. Manuel, R. Kisslinger, K. Alam, U. Thakur, N. Mahdi, P. Kumar, *Appl. Catal., B* **2019**, *243*, 522.
[42] H. Li, F.-Q. Shao, S.-Y. Zou, Q.-J. Yang, H. Huang, J.-J. Feng, A.-J. Wang, *Microchim. Acta* **2016**, *183*, 821.
[43] a) C. Di Valentin, G. Pacchioni, A. Selloni, *J. Phys. Chem. C* **2009**, *113*, 20543; b) Z. Lian, W. Wang, G. Li, F. Tian, K. S. Schanze, H. Li, *ACS Appl. Mater. Interfaces* **2017**, *9*, 16959.
[44] a) S. N. Habisreutinger, L. Schmidt-Mende, J. K. Stolarczyk, *Angew. Chem., Int. Ed.* **2013**, *52*, 7372; b) L. Jing, S. Li, S. Song, L. Xue, H. Fu, *Sol. Energy Mater. Sol. Cells* **2008**, *92*, 1030.
[45] F. E. Osterloh, *Chem. Soc. Rev.* **2013**, *42*, 2294.
[46] O. K. Varghese, C. A. Grimes, *Sol. Energy Mater. Sol. Cells* **2008**, *92*, 374.
[47] a) X.-Y. Zhang, A. Hu, T. Zhang, X.-J. Xue, J. Z. Wen, W. W. Duley, *Appl. Phys. Lett.* **2010**, *96*, 043109; b) A. Mohammadpour, K. Shankar, *J. Mater. Chem.* **2010**, *20*, 8474.
[48] S. Farsinezhad, A. Mohammadpour, A. N. Dalrymple, J. Geisinger, P. Kar, M. J. Brett, K. Shankar, *J. Nanosci. Nanotechnol.* **2013**, *13*, 2885.
[49] M. G. Walter, E. L. Warren, J. R. McKone, S. W. Boettcher, Q. Mi, E. A. Santori, N. S. Lewis, *Chem. Rev.* **2010**, *110*, 6446.
[50] a) C. Mao, F. Zuo, Y. Hou, X. Bu, P. Feng, *Angew. Chem.* **2014**, *126*, 10653; b) Z. Wang, B. Wen, Q. Hao, L.-M. Liu, C. Zhou, X. Mao, X. Lang, W.-J. Yin, D. Dai, A. Selloni, *J. Am. Chem. Soc.* **2015**, *137*, 9146.
[51] S. K. Cushing, F. Meng, J. Zhang, B. Ding, C. K. Chen, C.-J. Chen, R.-S. Liu, A. D. Bristow, J. Bright, P. Zheng, *ACS Catal.* **2017**, *7*, 1742.
[52] J. Su, L. Zhu, P. Geng, G. Chen, *J. Hazard. Mater.* **2016**, *316*, 159.
[53] a) A. G. da Silva, T. S. Rodrigues, V. G. Correia, T. V. Alves, R. S. Alves, R. A. Ando, F. R. Ornellas, J. Wang, L. H. Andrade, P. H. Camargo, *Angew. Chem., Int. Ed.* **2016**, *55*, 7111; b) J. Wang, W. Qiao, X. Mu, *Appl. Sci.* **2018**, *8*, 2026; c) A. P. Manuel, A. Kirkey, N. Mahdi, K. Shankar, *J. Mater. Chem. C* **2019**, *7*, 1821; d) X. Ren, E. Cao, W. Lin, Y. Song, W. Liang, J. Wang, *RSC Adv.* **2017**, *7*, 31189.
[54] T. You, L. Jiang, P. Yin, Y. Shang, D. Zhang, L. Guo, S. Yang, *J. Raman Spectrosc.* **2014**, *45*, 7.
[55] X. Yang, H. Yu, X. Guo, Q. Ding, T. Pullerits, R. Wang, G. Zhang, W. Liang, M. Sun, *Mater. Today Energy* **2017**, *5*, 72.
[56] P. Kumar, E. Vahidzadeh, U. K. Thakur, P. Kar, K. M. Alam, A. Goswami, N. Mahdi, K. Cui, G. M. Bernard, V. K. Michaelis, *J. Am. Chem. Soc.* **2019**, *141*, 5415.
[57] a) Q. Ding, Y. Shi, M. Chen, H. Li, X. Yang, Y. Qu, W. Liang, M. Sun, *Sci. Rep.* **2016**, *6*, 32724; b) E. Cao, M. Sun, Y. Song, W. Liang, *Nanotechnology* **2018**, *29*, 372001; c) L. Kang, J. Chu, H. Zhao, P. Xu, M. Sun, *J. Mater. Chem. C* **2015**, *3*, 9024.
[58] W. Lin, Y. Cao, P. Wang, M. Sun, *Langmuir* **2017**, *33*, 12102.
[59] a) B. Dong, Y. Fang, L. Xia, H. Xu, M. Sun, *J. Raman Spectrosc.* **2011**, *42*, 1205; b) S. Wu, Y. Liu, C. Ma, J. Wang, Y. Zhang, P. Song, L. Xia, *Langmuir* **2018**, *34*, 7240.
[60] J. Wang, W. Lin, X. Xu, F. Ma, M. Sun, *Chem. Rec.* **2018**, *18*, 481.
[61] Q. Ding, Y. Shi, M. Chen, H. Li, X. Yang, Y. Qu, W. Liang, M. Sun, *Sci. Rep.* **2016**, *6*, 32724.
[62] T. Siefke, S. Kroker, K. Pfeiffer, O. Puffky, K. Dietrich, D. Franta, I. Ohlídal, A. Szeghalmi, E.-B. Kley, A. Tünnermann, *Adv. Opt. Mater.* **2016**, *4*, 1780.
[63] V. B. Kumar, A. K. Sahu, A. S. M. Mohsin, X. Li, A. Gedanken, *ACS Appl. Mater. Interfaces* **2017**, *9*, 28930.